

HiSST: 4th International Conference on High-Speed Vehicle Science Technology

22-26 September 2025, Tours, France



Validation of an automated toolset for mesh adapted Navier-Stokes simulation of high speed vehicles

Mathieu Lugrin ¹, Baptiste Isnard ², Bruno Maugars ³, Cédric Content ⁴

Abstract

A fully automated toolset for Navier-Stokes and Reynolds Averaged Navier-Stokes computation around high speed vehicles is presented. It is based on a CAD-based automated meshing and anisotropic metric-based remeshing tool built on the REFINE toolbox, a node-centered Navier-Stokes in the SoNICS suite, and the maia library. The tool is validated on open cases representative of the complexity of the flow encountered around high-speed vehicles including reentry and airbreathing cruise vehicles. This includes complex three-dimensional forebody laminar simulations, turbulent shock-train for internal aerodynamics, and axisymmetric triconic cases. A demonstration on a full cruise vehicle, with a modeled scramjet engine, is then conducted and presented as an illustration of future possible use of the tool.

Keywords: Hypersonic, CFD, mesh-adaptation

1. Introduction

Proper design of high speed vehicles relies heavily on the use of CFD, mostly in the form of computation of steady Navier Stokes or Reynolds Averaged Navier Stokes solutions. Those computations give access to key performance indicators such as integrated data (e.g. lift to drag ratio, thrust, aerodynamic stability, etc...) or local quantities (heat fluxes, pressure load, ...) that are then used to evaluate and refine the designs. Even with recent advances in terms of tools and solvers, setting up a CFD computation from a CAD drawing of a system is still a time-intensive task that needs to be done by a skilled engineer. While the use of unstructured meshes has reduced quite drastically the human time required to build medium to high quality meshes, meshing remains one of the main blocking points towards the use of CFD in automated toolchains. As the aerospace industry continues to push for more efficient design, the necessity for automated CAD to post-process workflows becomes increasingly evident. The manual CAD to mesh process, which is prone to human error and time-consuming iterations, obstructs the overall productivity of engineering teams. An integrated, automated meshing solution would significantly streamline the CFD pipeline, enabling faster design evaluation and optimization. Anisotropic mesh adaptation represents a very promising solution to alleviate the manual meshing problems, it provides good convergence of the solution even with no physical intuition nor knowledge in the starting mesh. However, most toolchains relying on mesh adaptation are still not automated CAD-to-post workflows, as the tool often requires the creation of a manual surface mesh of the model and tagging of the boundary conditions. They are also often relatively inefficient (even if the mesh adaptation by itself allows for more efficient computation due to the lower amount of points needed to converge a solution) as they chain tools through I/O and different executables. Some of the tools are also not built to work in a parallel/distributed manner, which strongly limits performance, and worse, the maximal number of points that can be computed as one may reach the memory limit of the computing nodes.

This paper presents a fully automated, parallel distributed CAD to POST toolset for NS and RANS computation based on anisotropic mesh adaptation. To assess its ability to capture the flow around high-speed vehicles, the tool is tested on open cases representative of the complexity of the flow encountered in real-life applications, such as canonical reentry vehicle, complex 3D forebody, and supersonic internal aerodynamics. Finally, a demonstration on a full cruise vehicle is conducted.

¹DAAA, ONERA, Institut Polytechnique de Paris, 92190 Meudon, France, mathieu.lugrin@onera.fr

²DAAA, ONERA, Institut Polytechnique de Paris, 92190 Meudon, France

³ DAAA, ONERA, Institut Polytechnique de Paris, 92320 Châtillon, France

⁴DAAA, ONERA, Institut Polytechnique de Paris, 92320 Châtillon, France

2. Toolset description

The toolchain (presented in figure 1) is built based on two main tools, namely a node-centered Navier-Stokes solver based on the SoNICS solver from ONERA-SAFRAN and an anisotropic mesh adaptation toolbox adapted from the open-source toolbox REFINE developed by NASA [2]. The input of the tool is a CAD description of the volume of fluid to simulate or of the unsewed surface patches (in STEP format); the surfaces of the CAD files are named according to the family of BCs that need to be tagged using the advanced face option of the STEP format.

First, the STEP files is read using EGADS and fed to REFINE to produce a surface mesh; a volume mesh is then created using either netgen or tetgen. This volume mesh then enters the SoNICS environment to tag BCs (automatically based on the names of the CAD surfaces), initialize the flow, and add a reference state, everything is stored in a CGNS compliant python tree representation. The tree is partitioned automatically so that the parallelization of all the steps is completely transparent to the user. Every step is linked through a memory API so that no IO has to be conducted.

Steady compressible Navier-Stokes or RANS computation are then conducted using the node centered solver of SoNICS. The spatial discretization is based on the one proposed by A. Dervieux and C. Debiez [5] on simplex mesh (triangle/tetrahedron). The convective terms are solved by the finite volume method on the dual mesh composed of median cells. Fluxes are determined through the use of the AUPM approximate Riemann solver proposed by Chen *et al.* [4]. Second order space accuracy is achieved through MUSCL type reconstruction method [12]. The MUSCL procedure is applied as proposed in A. Dervieux and C. Debiez [5] or Alauzet and Frazza [1] to recover the so-called V4-scheme. A shock capturing similar to the one of [9] is also implemented. Viscous fluxes are computed with the conventional expression described as Cell Based Viscous scheme in Liu *et al.* [7]. Boundary conditions are weakly imposed by evaluating the flux at each facet on the borders of the domain. As in Alauzet and Frazza [1], each Dirichlet boundary (such as the velocities on a no-slip wall) are strongly enforced at each iteration *ie.* the DOF concerned by the boundary are removed from the whole CFD problem. Time integration is conducted using a backward euler scheme using an efficient implicit LU-SGS solver. For RANS computation, the Spalart-Allmaras (SA) [11] model with the compressibility correction of [6] and the Quadratic Constitutive Relation (QCR) [10] is used.

Once a solution is converged, the mesh is adapted using a metric based on a Mach number hessian, a gradation parameter and an enhanced treatment of the wall computed inside the solver. The metric is then passed to REFINE to conduct anisotropic mesh adaptation. To ensure that the initial CAD is respected, the refined surface mesh is reprojected directly on the CAD. Once the new mesh is available, the previous solution is interpolated on the new mesh and the computation is run again, solution computation and remeshing steps are looped until a proper solution is converged. Everything is done from a single python script that takes as inputs the step file and the run conditions. All pre/post-processing, partitioning and distribution are done using the open source MAIA library (https://github.com/onera/Maia).

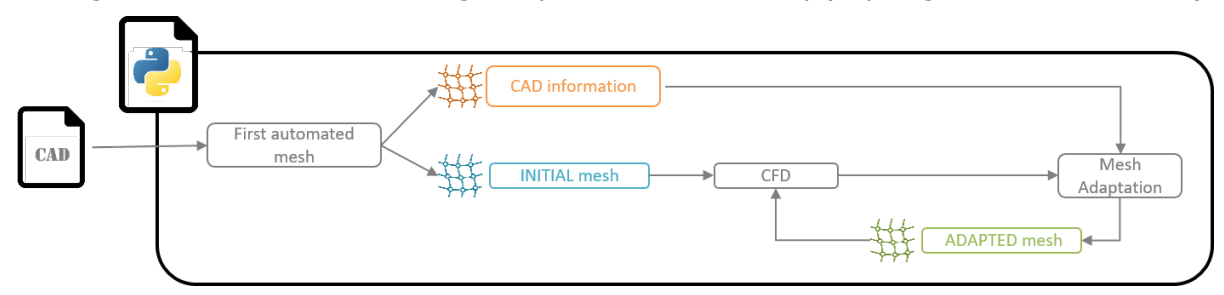


Fig 1. Schematic of the toolchain used for the automated computations.

3. Reentry vehicles

The first type of high-speed vehicles of interest are the reentry vehicles. To assess the ability of the solver to treat those cases, the axisymmetric cone-cylinder-flare CCF12 geometry, which was designed as a canonical and open case to study the flow features found in atmospheric reentry vehicles is chosen as a benchmark. It includes a simple developing hypersonic laminar boundary layer followed by more complex features such as boundary layer interaction with expansion fans, and most importantly, separation induced by the shock-boundary layer interaction. The numerical results of Caillaud et al. [3] are used

as a reference.

In that specific 2D axisymmetric case, the step file is generated from the analytical description of the body using GMSH. An example of an adapted mesh on that case, alongside a Mach number contour, is presented in figure 2. Taking the low Reynolds case as an example, the toolset is run for 121 seconds on 4



Fig 2. Adapted mesh and Mach number contour for the low Reynolds number case of [3]

cores of an Intel Cascade Lake CPU, allowing us to conduct 6 mesh adaptations and steady computations until complete convergence is reached, the evolution of the wall pressure distribution for each step is presented in figure 3.

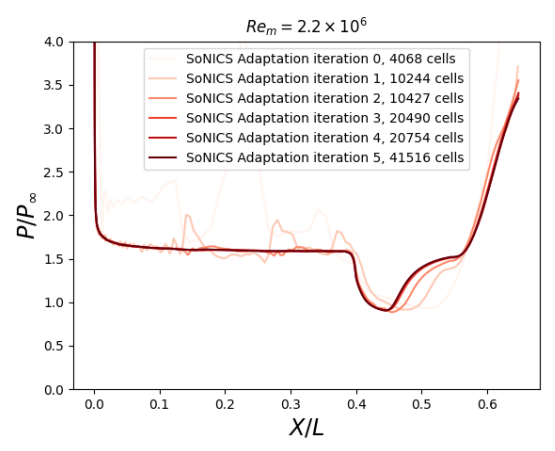


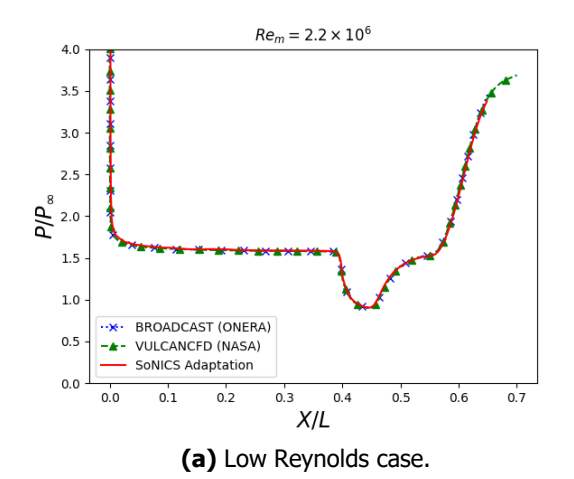
Fig 3. Evolution of the wall pressure distribution on the CCF12 at low Reynolds number at each iteration showing the convergence path.

The wall pressure distribution for two different Reynolds numbers is presented in figure 4 alongside results from two high-order solvers. Given the sensitivity of the strongly separated shock boundary layer interaction to both the resolution of the boundary-layer gradients and the associated separation and reattachment shock, getting the correct pressure signature guarantees that they are accurately captured in the solution. This result validates the good behavior of the toolset for hypersonic axisymmetric configurations. Note that the high Reynolds case from [3] is not shown here as it is highly unstable and requires special stabilized time integrators or even a Newton method to be able to capture a steady state.

Follow-on steps for that case would be to extract the Jacobian operator from the solver using algorithmic differentiation and compare stability results. Mesh adaptation based on the convergence of either the eigenvalues of the Jacobian or of the Resolvent operator could also be conducted. Once the Jacobian is available, a Newton method could also be used to capture the high-Reynolds baseflow.

4. Cruise vehicles

The second type of vehicle of interest is air-breathing cruise vehicles, which, in addition to external aerodynamics, involve complex internal flow as well as control surfaces. Given the sparsity of open full validation cases for such air-breathing vehicles, the validation is done by splitting the vehicle into subcases of interest, for which we can find open validation cases, namely, the forebody for external



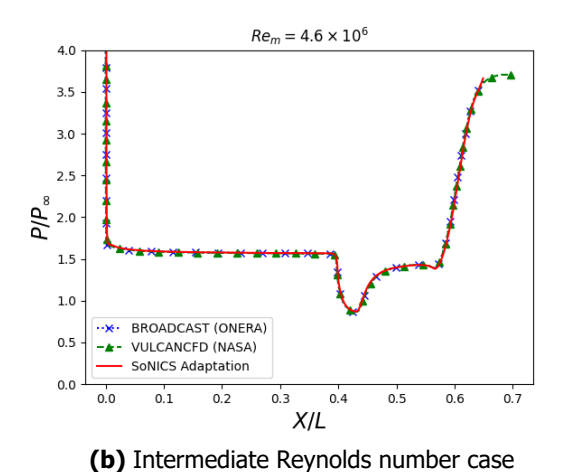


Fig 4. Wall pressure distribution for the CCF12 geometry at Mach 6 for two different Reynolds number alongside reference data from [3].

aerodynamics and a shock-train case for internal aerodynamics. Then a demonstration is conducted on a mock-up full vehicle.

4.1. Forebody

The first subcase of interest concerns forebodies, which are often complex 3D geometries on which the main problematic will be drag, lift and heat-flux prediction. The BOLT case is chosen as it provides plenty of open data (including flight) and its 3D geometry is representative of the complexity of real designs. It also displays an intricate baseflow structure with multiple vortices, which is challenging to capture and is thus a good benchmark. The chosen condition for the computation is a challenging high Reynolds case with both CFD and sparse flight data coming from [13]. This case is at a flight altitude where laminar-turbulent transition starts to appear (around 20km), which means that it is the highest Reynolds number for which the flow remains laminar. It is thus fully representative of a scale one forebody flying at cruise altitude. This case would also serve future validation of transition prediction tools integrated to the solver.

The case is run on a quarter of the full scale flight BOLT II model using symmetry planes. The computation is conducted on 2400 intel Cascade Lake cores for a single job of 15 hours, allowing to conduct 8 adaptation/computation steps and to reach a final mesh of 360M cells in order to reach proper convergence of the wall heat-fluxs. It is interesting to mention here that convergence of wall heat-fluxes is way harder to reach compared to other figures of merit such as wall pressure distribution.

An illustration of the geometry alongside wall heat-flux distribution and a Mach number field at the outlet of the domain are presented in figure 5. It highlights the complex nature of the flowfield with multiple vortical structures appearing, especially in the center region. Quantitative comparison of heat-fluxes at two different longitudinal with the CFD solution of [13] are presented in figure 6. Overall excellent agreement is found between the two simulations. Results from the mesh adaptation display a relatively good smoothness given that they come from anisotropic tetrahedron only meshes. Some discrepancies are still visible in the peaks linked with local vortices, mostly in terms of amplitude of the fluctuation. The origin of those discrepancies is still unknown; they may be linked to differences in the mesh resolution; some vortices may be under-resolved in either simulation. Another possible origin would be vortices growth linked with numerical error coming from the time integrators, as the baseflow is extremely unstable; small numerical errors could lead to the growth of structures which are not part of the baseflow. Future work on that case would require other simulations coming from other meshes and/or solvers to assess the origin of those discrepancies. Again, a Newton method could be used once the Jacobian operator is available to compute a fixed point of the equations.

Overall, the tool appears to be fully capable of computing a very complex baseflow such as the one encountered on the BOLT forebody. The key point to highlight here is that the user time needed to set up such a computation is minimal (of the order of minutes) with no effort whatsoever put into meshing, which strongly contrasts with other studies on that case.

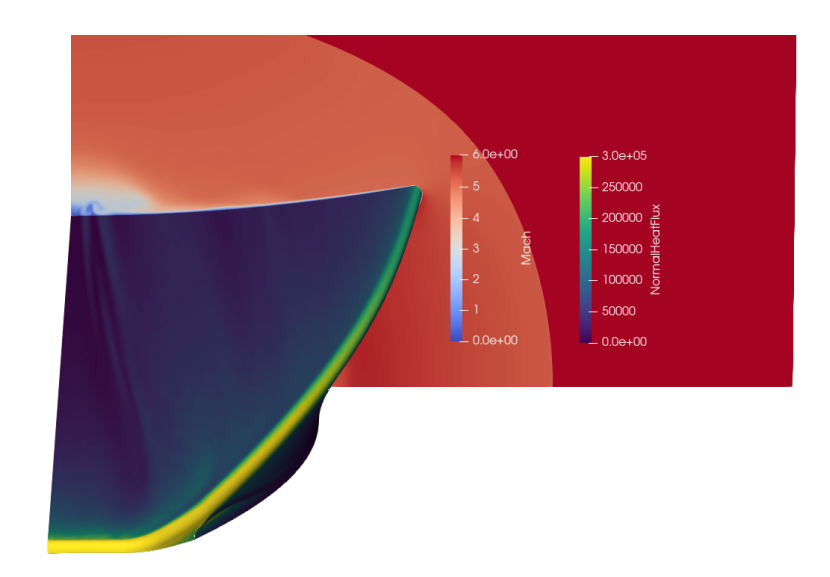


Fig 5. BOLT geometry and simulation results for the descent case of [13].

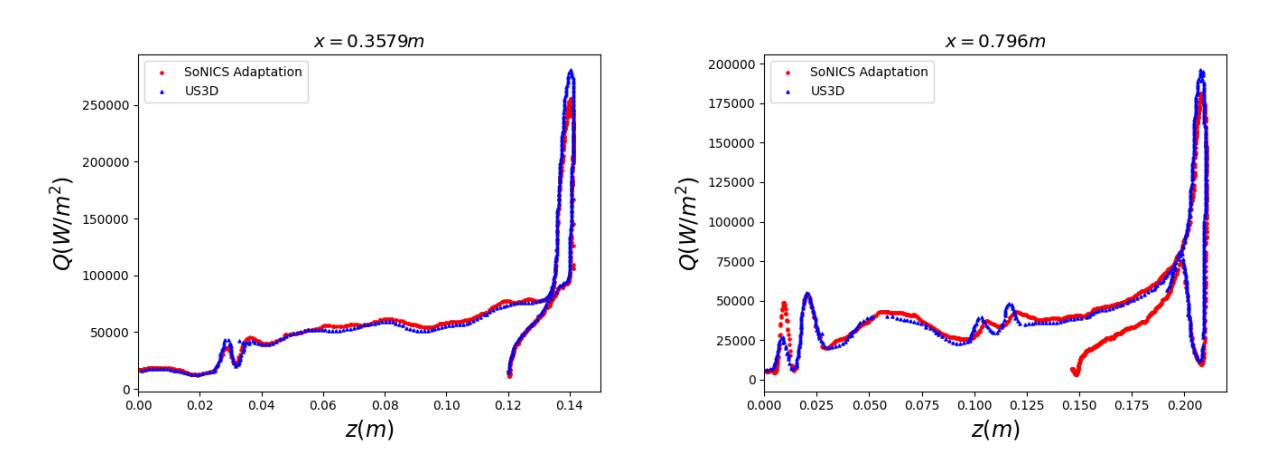


Fig 6. Spanwise heat-fluxes distribution at two longitudinal section of the BOLT forebody alongside data from the US3D computation of [13].

4.2. Internal aerodynamics

To assess the ability of the solver to capture supersonic internal aerodynamics, a canonical reference case from ONERA is used. The case is built to represent the complexity of real dual mode ramjet applications. It consists of a square duct with straight, converging, and then slowly diverging sections, followed by a choked nozzle. As such, it includes corner flows and multiple shock-boundary layer interactions, creating a shock train leading to a fully developed separated flow. Flow conditions for that case are presented in table 1.

Table 1. Reference conditions for the computations.

M_{∞}	P_{∞}	T_i	α	β
3	4000 Pa	300 K	0°	0°
	T _{wall}	Re _L	L	
	300 K	4.029×10^{6}	0.4 m	

To provide a reference for this case, a Direct Numerical Simulation is run (see figure 7); flow conditions are presented in table 1. The DNS is performed using the open-source HPC oriented FAST compressible

Navier-Stokes solver from ONERA (https://onera.github.io/Fast/) on a 3.5 billion points mesh (see table 2). The numerical method is based on an improved version of the low dissipation AUSM of [8] and a fifth order MUSCL reconstruction alongside the shock-capturing technique of [9], viscous fluxes are computed using a second-order accurate centered scheme. Time integration is performed via an explicit low-storage third-order 3-step Runge-Kutta scheme; the time step is set to $\Delta t = 3 \times 10^{-9} s$ to ensure a CFL number lower than 0.5 in the whole domain. The computation was run using a hybrid MPI/OpenMP parallelism on 64 computing nodes (3072 cores), using 1024 MPI processes and 3 OpenMP threads per process. The mean flow is averaged over 2 \times 10⁶ iterations, which corresponds to a physical time of 6ms. The full description of this computation is out of the scope of the paper; geometry and mean flow are available upon request to the authors.

Table 2. Mesh characteristics

DNS						
n_{x}	n_y	nz	n_{tot}	Δx_{max}^+	Δy , z_{max}^+	$\Delta y, z_{wall}^+$
9807	605	605	3.59×10^{9}	< 12	< 10	< 1.4

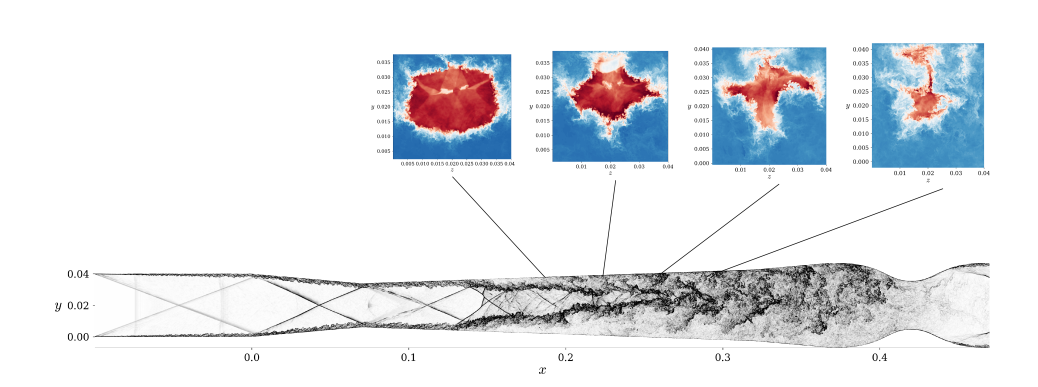


Fig 7. Illustration of the internal aerodynmaics reference simulation thanks to instantaneous numerical pseudo-schlieren in a constant z-plane (z = 0.01) of the configuration and instantaneous stagnation pressure contour in various x-plane.

In addition to the DNS data, and to compare the results of the automated toolset with standard best-practice engineering procedure, a RANS computation is also performed using the elsA software (ONERA-Safran property) on a coarse version of the DNS mesh.

The time-averaged Mach number fields (in the central plane) for the DNS and both RANS computations are presented in figure 8. The flow displays all the main expected features: first, a boundary layer develops, then encounters a first shock wave as it reaches the compression ramp, followed by an expansion at the entrance of the diffuser. The flow ends up separating through a SBLI and is slowed down by a shock train to finally reach a purely subsonic state. Both RANS computation display results that are surprisingly close to the DNS reference given the complexity of the flow (one can note here that the use of the QCR strongly improves the quality of the RANS solution). From an engineering perspective both method would be acceptable for vehicle design. This validates the good behavior of the toolset for turbulent internal aerodynamics. Looking closer at the solutions, one can notice that the elsA computation results display a shock train that is located closer to the top wall than the mesh-adapted one; the latter is thus closer to the DNS reference. This may be due to the traditional meshing procedure used for the standard simulation, where the mesh is highly refined near the walls to properly capture the boundary layer, leading to a mesh-induced displacement of the shock train. As the refinement of the mesh-adapted simulation is fully feature-driven, no such best practice is used, which leads to a better

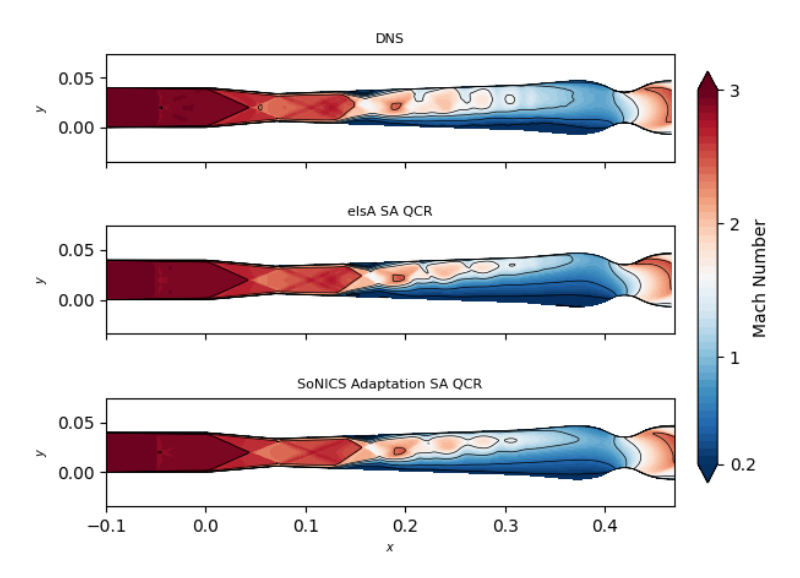


Fig 8. Mach number distribution in the central z-plane. The DNS results correspond to time-averaged flow.

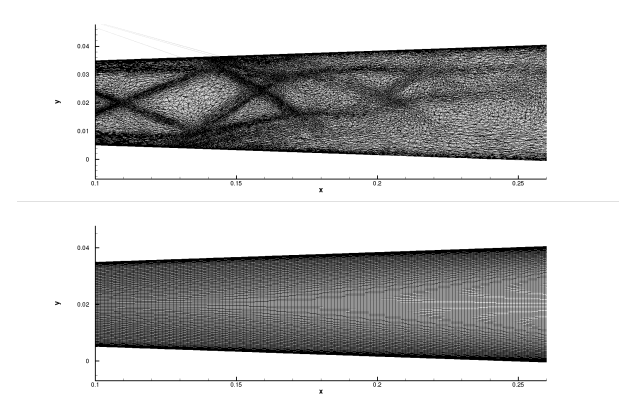


Fig 9. Meshes from the adapted (top) and elsA (bottom) SA QCR simulations in the central plane for the shock-train region.

resolution of the mesh further away from the wall. The difference between both meshes in the central plane for the shock train region is displayed in figure 9. The adapted mesh clearly displays a refined region further away from the wall in addition to the near-wall refinement for the boundary layer, which may allow a better capture of the physics of the flow.

4.3. Full vehicle simulation

Now that the ability of the toolset to capture both complex internal and external high speed aerodynamic flowfield has been documented, a demonstration on a full mock-up vehicle can be conducted. The case consists of a high Mach number cruise of a scramjet powered vehicle. The combustion chamber is not computed but replaced by a 0D model from the throat of the air intake to the entrance of the nozzle. This computation only serves as a demonstration of how we can leverage the ability of the toolset to handle complex geometry at no additional cost. Setup time for such a computation takes less than one hour of human work. The toolset is then run on 600 Intel Cascade Lake cores for a single job of 15 hours, which allowed conducting 12 adaptation/computation steps to reach convergence; the final mesh has 208M cells. Samples of results are presented in figures 10 and 11. While quantitative data cannot be shown here, the purpose is to demonstrate the ability of the tool to handle complex geometries (control surfaces, bleed system), one big advantage being that geometric variability is fully transparent to the user, the same computation could be launched with different control surfaces or even additional ones

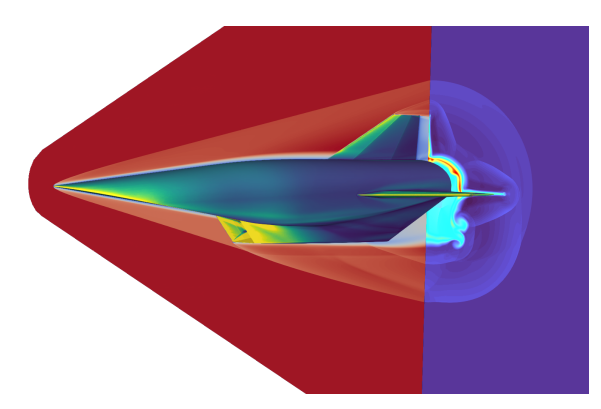


Fig 10. Skin-friction, Mach number slice in the central plane and temperature slice at the outlet illustrating the external aerodynamics of the full vehicle.

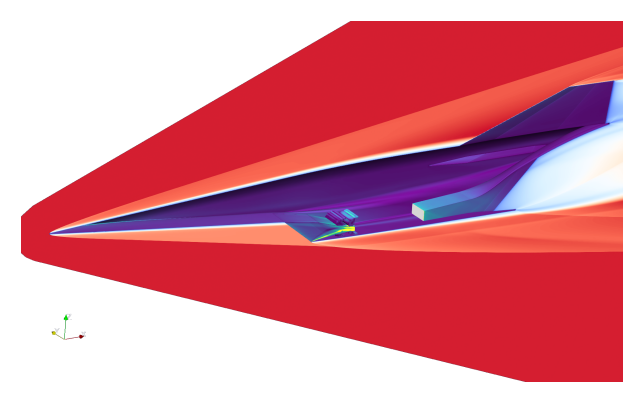


Fig 11. Skin pressure distribution and Mach number slice in the central plane illustrating the internal aerodynamics of the full vehicle.

for instance using the exact same script just by changing the input CAD file.

5. Conclusion

This study marks a significant milestone in the development of computational tools for high-speed vehicle design, as we successfully presented and validated a comprehensive toolchain for automated CAD to post mesh-adapted Navier-Stokes simulations around complex high-speed vehicles. The tool could also be used for other lower-speed computations.

Computations were conducted on open cases from the literature to assess the tool performance, ensuring its reliability in capturing complex flow phenomena characteristic of high-speed vehicle applications. Building upon this solid foundation, a demonstration on a complete vehicle geometry showcased the toolchain's versatility and effectiveness in handling real application design features.

Acknowledgment

This project was provided with computer and storage resources by GENCI thanks to the grant 2023-A0142A14106 on the SKL partition of the supercomputer Irene at TGCC.

This work was partially supported by the DGAC SONICE project.

The authors wish to thank the DTIS department of ONERA for providing the full vehicle geometry as well as the DMPE department for providing the scramjet model.

References

1. Alauzet, F. & Frazza, L. Feature-based and goal-oriented anisotropic mesh adaptation for RANS applications in aeronautics and aerospace. Journal of Computational Physics 439, 110340. ISSN:

- 0021-9991. https://www.sciencedirect.com/science/article/pii/S0021999121002357 (2021).
- 2. Balan, A., Park, M. A., Wood, S. & Anderson, W. K. Verification of anisotropic mesh adaptation for complex aerospace applications in AIAA scitech 2020 forum (2020), 0675.
- 3. Caillaud, C. et al. Separation and Transition on a Cone-Cylinder-Flare: Computational Investigations. AIAA Journal 0, 1–20 (0).
- 4. Chen, S.-s., Yan, C., Zhong, K., Xue, H.-c. & Li, E.-l. A novel flux splitting scheme with robust-ness and low dissipation for hypersonic heating prediction. International Journal of Heat and Mass Transfer 127, 126–137. ISSN: 0017-9310. https://www.sciencedirect.com/science/article/pii/S0017931017354819 (2018).
- 5. Debiez C; Dervieux, A. Mixed-element-volume MUSCL methods with weak viscosity for steady and unsteady flow calculations. English. Computers & fluids. ISSN: 0045-7930 (2000).
- 6. Deck, S., Duveau, P., d'Espiney, P. & Guillen, P. Development and application of Spalart–Allmaras one equation turbulence model to three-dimensional supersonic complex configurations. Aerospace Science and Technology 6 (2002).
- 7. Liu, Y. et al. Edge-Based Viscous Method for Mixed-Element Node-Centered Finite-Volume Solvers. AIAA Journal 62, 209–230. eprint: https://doi.org/10.2514/1.J062996.https://doi.org/10.2514/1.J062996 (2024).
- 8. Mary, I. & Sagaut, P. Large Eddy Simulation of Flow Around an Airfoil Near Stall. AIAA Journal 40, 1139–1145. https://doi.org/10.2514/2.1763 (2002).
- 9. Sciacovelli, L., Passiatore, D., Cinnella, P. & Pascazio, G. Assessment of a high-order shock-capturing central-difference scheme for hypersonic turbulent flow simulations. Computers & Fluids 230, 105134 (2021).
- 10. Spalart, P. R. Strategies for turbulence modelling and simulations. International Journal of Heat and Fluid Flow 21, 252–263. ISSN: 0142727X (2000).
- 11. Spalart, P. R. & Allmaras, S. R. One-equation turbulence model for aerodynamic flows. Recherche aerospatiale 439, 5–21. ISSN: 00341223 (1994).
- 12. van Leer, B. Towards the Ultimate Conservative Difference Scheme. Journal of Computational Physics 135, 229–248. ISSN: 0021-9991 (1997).
- 13. Vu, C., Knutson, A., Subbareddy, P. K. & Candler, G. V. Postflight Receptivity and Transition Analysis of BOLT-II Side A Descent Trajectory in AIAA SCITECH 2024 Forum (2024), 0703.